Effect of local structural disorder on lithium diffusion behavior in amorphous silicon

Wenwen Li and Yasunobu Ando*

Research Center for Computational Design of Advanced Functional Materials, National Institute of Advanced Industrial Science and Technology, Tsukuba, Ibaraki 305–8568, Japan

(Received 30 January 2020; accepted 6 April 2020; published 28 April 2020)

Lithium-ion batteries with amorphous silicon (*a*-Si) anodes exhibit very high theoretical energy capacity, with the lithium kinetic transport having the most crucial effect on the battery performance. In this study, the lithium diffusion pathways in a series of large-scale *a*-Si models (512 atoms) with various extents of structural order are calculated using the machine learning interatomic potential. Then, the Li diffusion behavior in different atomistic environments is estimated from the transient state theory. The Li diffusion activation energy is observed to be lower (higher) in an ordered (disordered) local environment. The activation energy varies within the range of 1.21–1.46 eV, which agrees well with experimental measurements, 1.38–1.46 eV. Our simulations also show that Li diffusion is enhanced at higher Li concentration, which is consistent with experimental observations. The effects of structural disorder and Li concentration can be explained by the "trap" mechanism. Finally, we show that the sources of Li diffusion traps are dangling bonds and large voids in the *a*-Si matrix with the help of first-principles calculations. Our work provides insight into the Li diffusion mechanism, which is beneficial for improving the performance of *a*-Si anodes for lithium-ion batteries. In addition, we demonstrate the significant dependence of the ion transport behavior on the local atomic environment, which will be useful for future theoretical studies of technologically important amorphous materials beyond Si.

DOI: 10.1103/PhysRevMaterials.4.045602

I. INTRODUCTION

Silicon plays an important role in Li storage in high-capacity electrodes for next-generation lithium-ion batteries because of its very high theoretical gravimetric capacity (∼4200 mAh/g), which is approximately 11 times higher than that of graphite (∼372 mAh/g) [1,2]. Amorphous silicon (*a*-Si) is of interest because of its much higher robustness as an anode material during the initial lithiation/delithiation cycle than its crystalline counterpart [3]. In addition, *a*-Si can be fabricated in the form of a thin film using sputter deposition methods to create thin-film batteries. The kinetics of Li diffusion is an issue of central importance to the lithiation and delithiation of *a*-Si electrodes. The Li diffusion in *a*-Si determines the charging/discharging times, maximum capacity, self-discharge, power density, and cycling stability. Consequently, a fundamental understanding of the atomic transport mechanism is highly desirable.

Many previous experiments have been conducted to determine the Li diffusivity in *a*-Si electrodes using cyclic voltammetry [4,5], electrochemical impedance spectroscopy [6,7], the potentiostatic or galvanostatic intermittent titration technique [6–8], and secondary ion mass spectrometry (SIMS) [9–12]. The measured diffusivities span four orders of magnitude between 10^{-14} and 10^{-10} cm^2/s. This large discrepancy may originate from the various experimental measurement methods used and the very different Li concentrations (the Li concentration x varies across the large range of 0.05–3.6 in different experiments). These factors make understanding of the Li diffusion mechanism very difficult. Schmidt *et al.* used SIMS to estimate the Li tracer diffusivity in *a*-Si with relatively low Li contents ($x = 0.02$ and 0.06), which provided valuable information that is especially important for the initial lithiation stages. [10] The Li diffusion has an activation energy of (1.42 ± 0.03) eV, and the more Li-rich samples possessed diffusivities that were one order of magnitude higher. A trap-limited diffusion mechanism was suggested, explaining this result as stemming from a lower concentration of unsaturated traps.

In addition, several theoretical studies have provided insight into Li diffusion using atomistic simulations. One such study was performed by Tritsaris *et al.*, who used density functional theory (DFT) calculations to determine the Li interstitial positions and diffusive pathways [13]. Similarly, Yan *et al.* characterized the pathway network of Li in *a*-Si using the modified embedded atomic method (MEAM) force field and estimated the Li diffusivities using kinetic Monte Carlo (KMC) simulations [14]. Johari *et al.* simulated the lithiation process using *ab initio* MD and determined the Li diffusivity in Li_xSi alloy ($x = 1.0 - 3.75$) [15]. Recently, Chang *et al.* investigated the microstructure and concentration dependence of diffusion coefficients for Li in *a*-Si using MEAM force field calculations and KMC simulations [16]. However, because of the high computational demands, *ab initio* calculations are limited to small supercells and short simulation times. In addition, the aforementioned theoretical studies failed to consider realistic factors, such as the Li concentration and structural characteristics of the *a*-Si matrix.

Recently, a method involving the construction of interatomic potentials using machine learning (ML) has attracted

*Author to whom correspondence should be addressed: yasunobu.ando@aist.go.jp

considerable attention as a promising way to achieve high computational accuracy and speed [17–23]. In this method, ML potentials are "trained" using the results of *ab initio* calculations as the reference data for the learning process. The ML potential is then capable of predicting structural energies that are not included in the training dataset. Much higher accuracy can be achieved using ML-based interatomic potentials than conventional interatomic potentials with simple formulas. The ML techniques used for this method include neural networks (NNs), [17,24–38] kernel regression, [22,23,39] Gaussian process regression, [19,30,40–42], and linear regression [43–45]. Some very recent research demonstrated the great promise of ML potentials to elucidate the structures and properties of technologically important amorphous materials [25,33,40,43]. For example, both Deringer's [40] and our previous work [33] showed that large-scale *a*-Si models containing 512–4096 atoms can be generated using different high-accuracy ML interatomic potentials (Deringer's case: Gaussian approximation potential and our work: high-dimensional neural network potential). High-quality *a*-Si models that match experimental samples prepared using different annealing processes (various extents of structure disorder) were generated in our previous work [33]. In another of our previous works, we showed that the neural network (NN) potential accurately estimates the Li diffusivity in amorphous Li_3PO_4 [25].

Large-scale *a*-Si models with various degrees of structural disorder were adopted in this work to investigate the effect of local structural order and Li concentration on the ion diffusion behavior in *a*-Si and provide deeper insight into the diffusion mechanism. In this work, a sequence of methods was employed to unambiguously determine the network of the diffusive pathways in *a*-Si models. Then, in conjunction with the KMC algorithm that allows multiparticle motion, we evaluated the important properties of Li diffusion, including the diffusion coefficient and activation energy. Our simulation results are consistent with the experimental results of Schmidt *et al.* [10] and provide theoretical support for the "trap" mechanism. Finally, the source of the Li "trap" was analyzed with the help of first-principles calculations. In comparison with the previous theoretical research, this work adopted much larger *a*-Li_xSi models, which can accurately reproduce the structural, vibrational and energetic properties of experimental *a*-Si samples [33]. More importantly, this work shows that degrees of structural order of the amorphous matrix has a significant influence on ionic diffusion behavior in it, which was not addressed in the previous theoretical and experimental research.

II. COMPUTATIONAL DETAILS

A. High-dimensional NN potential

In the present work, the Behler-Parrinello scheme of the high-dimensional NN potential [46] was constructed for the Li/Si binary system and used as the force field for the following atomistic simulation. The basic idea of the NN potential is that the total energy of a structure E_{total} can be expressed as the sum of energy contributions of respective atoms E_i, and each energy contribution can be predicted by the individual atomic NN according to the local atomic environment of the atom:

$$E_{\text{total}} = \sum_{i}^{\text{Natoms}} E_i.$$

The many-body symmetry functions proposed by Behler *et al.* [47] were used as the descriptors of the local atomic environment, i.e., the inputs of atomic NNs. The formulas of the symmetry functions are provided in the Supplemental Material [48].

Construction of an NN potential requires a large number of *ab initio* calculations to generate reference data. The *ab initio* calculations were performed using the Vienna *Ab initio* Simulation package (VASP) [49,50]. The projector augmented wave method was used to treat the atomic core electrons, and the Perdew-Burke-Ernzerhof functional within the generalized gradient approximation was used to describe the electron-electron interactions [51,52]. The reference database contains both pure Si and Li/Si binary structures, with the supercell size varying from 8 to 129 atoms. The cutoff energy for the plane-wave basis set was set to 550 eV. The *k*-point mesh for the *ab initio* calculations is provided in the Supplemental Material [48].

One important issue for NN potential construction is the sampling of reference structures. Many different approaches to sampling training data have been suggested, including the bootstrap method [53] and comparison of structure similarity [54]. In this work, we employed the adaptive learning scheme by exploiting the high flexibility of NNs (the details are provided in our previous work [33]). In the adaptive learning scheme, atomistic simulations are performed based on either NN potential prediction or *ab initio* calculations depending on the circumstances [54–57]. More precisely, two NN potentials (with different NN configurations) are generated and used to perform MD or nudged elastic band (NEB) simulations. The *ab initio* calculation is performed if the "disagreement" between the two ML models is large, and the *ab initio* calculation results are then added to the reference database to improve the NN potentials. In general, the adaptive learning scheme constantly explores the potential energy surface (PES) to find and reinforce the "weak points" of the reference database. The reference database contains *a*-Si data used in earlier work [33], which was sampled from repeatedly adaptive learning MD runs at 300–2500 K. In addition, the Li/Si binary structures were sampled in two ways. Some of the binary structures were selected from the adaptive learning MD runs at 300–1200 K. The other binary structures were Li diffusion transient images that sampled from the adaptive learning NEB calculations. Our earlier work in calculating the diffusion properties of *a*-Li_3PO_4 proved that these transient structures are critical for the accurate reproduction of Li diffusion barriers [25]. The high-dimensional neural network potential was trained using a homemade package (Data-driven atomistic Interaction Modeling Package: DIMP).

B. Unambiguous construction of diffusive network

To obtain atomistic-level insight into the interstitial diffusion mechanism in amorphous materials, the following basic information is necessary: (1) the stable interstitial positions,

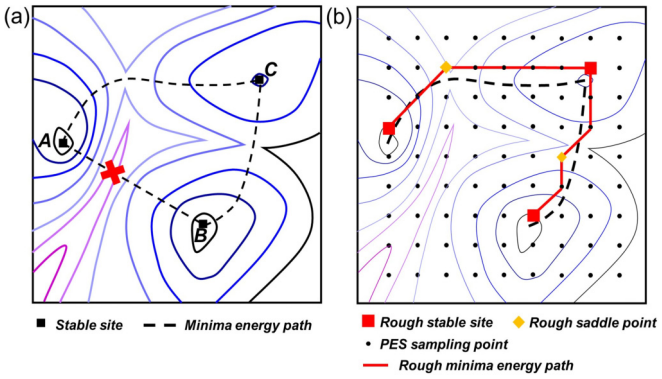

FIG. 1. Illustration of Li diffusion potential energy surface in amorphous silicon.

(2) the connectivity of the interstitial positions, and (3) the diffusive pathways and their barrier energies. This information makes up the *diffusive network* of the interstitial atom. In previous studies, the interstitial position has been predetermined from physical intuition [13] or relaxed from arbitrary positions [24,58]. However, the former method cannot guarantee that all the possible interstitial sites are taken into account, whereas the latter method requires much more computational effort. More importantly, the determination of connectivity, i.e., which pair of interstitial sites the diffusing atom can directly hop between, is not straightforward. A simple approach is to consider a pair of sites closer than a certain cutoff distance to be connected [24,25]. However, there is no clear method to determine this cutoff distance, and the connectivity does not simply depend on the spatial distance. As observed in Fig. 1(a), sites A and B are spatially close. However, the Li atom cannot directly hop from A $\rightarrow$ B but instead hops from A $\rightarrow$ C $\rightarrow$ B because of the special shape of the PES. Such a problem can be manually identified by the presence of two clear peaks in the energy profile along the diffusion pathway. However, because of the existence of thousands of diffusion pathways in our large-scale *a*-Si models, an unambiguous and thorough search method for the diffusive network is needed.

One possible way to address this problem is to use the autonomous basin climbing (ABC) method, which is a method for sampling and reconstructing the system's PES developed recently by Kushima *et al.* as an adaptation of the concept of metadynamics [14,59]. The ABC algorithm can provide a "reasonable" approximation of the PES by adding a Gaussian penalty function to the energy-minimized structures followed by relaxation. The approximated PES is used to estimate the diffusive network. In this work, we constructed the diffusive network by presampling of the PES. More specifically, a Li atom was inserted at each of the points defining a $N \times N \times N$ uniform grid in the *a*-Si matrix supercell, and then, the configuration was optimized with a fixed Li atom. A three-dimensional approximated PES of the Li atom was obtained from the final potential energy after relaxation. As shown in Fig. 1(b), we can recognize the rough stable/saddle points and the site connectivity from the PES. The accuracy of the PES can be improved by using more sampling grid points; however, this strategy results in a significant increase in computational cost. In this work, the interval of the grid points was set to 0.3 Å. Then, the full optimization and NEB method is applied to the output of the PES analysis to obtain accurate interstitial positions, diffusion pathways, and energy barriers.

C. Multi-particle-diffusion kinetic Monte Carlo

The KMC algorithm has been extensively used to simulate the interstitial diffusion process in amorphous materials when the diffusive network is known. However, in most previous studies, the diffusion of a single particle was simulated without consideration of particle concentration [14,24,58]. In a previous experiment, it was shown that the Li concentration has a great effect on its diffusivity in *a*-Si [10]. To understand the effect of Li concentration, we adopted the multiparticle KMC algorithm.

In the multiparticle algorithm, more than one Li atom simultaneously exists in the diffusive network, and a Li atom cannot hop to a site that is already occupied. For example, three Li atoms are situated at the i^{th}, j^{th}, and k^{th} sites of the diffusive network. The Li atom at the i^{th} site cannot hop to the j^{th} and k^{th} sites even if they are topologically connected to the i^{th} site. Thus, the possible Li occupation sites in the next step are

$$(i,\ j,\ k) \rightarrow \begin{cases} (i',\ j,k) & [i' \in N^i;\ i' \neq j,k] \\ (i,\ j',k) & [j' \in N^j;\ j' \neq i,k] \\ (i,\ j,\ k') & [k' \in N^k;\ k' \neq i,\ j] \end{cases},$$

where N^i, N^j, and N^k are the sets of neighboring sites connected to the i^{th} <, j^{th} and k^{th} sites, respectively, in the diffusive network. The probability of Li occupation sites changing from (i, j, k) to (i', j, k) in a certain period can be expressed as

$$P_{ijk\rightarrow i'jk} = \nu \exp\left(-\frac{\Delta E_{ii'}}{k_B T}\right),$$

where $E_{ii'}$ is the barrier energy of the diffusion path i to i', ν is the vibration frequency (10^{13}/s), and k_{B} is the Boltzmann constant. The residual time that Li atoms occupy (i, j, k) is

$$\tau = \frac{1}{\sum_{i' \in N^i}^{i' \neq jk} P_{ijk\rightarrow i'jk} + \sum_{j' \in N^j}^{j' \neq ik} P_{ijk\rightarrow ij'k} + \sum_{k' \in N^k}^{k' \neq ij} P_{ijk\rightarrow ijk'}}.$$

The multiparticle KMC algorithm is illustrated in Fig. 2.

It should be stressed that the algorithm does not precisely account for the Li-Li interaction. The presence of a Li atom at one site will affect the shape of the surrounding PES; however, the algorithm neglects this effect, which will affect the accurate simulation of the collective motion of atomic clusters to some extent. The KMC method also assumes that the structure of the *a*-Si matrix does not change during the Li diffusion process. Our KMC method is applicable because we mainly focus on the Li diffusion behavior at low temperature in this work. To study diffusion process at high temperature, we should consider the thermal effect carefully since the collective motion between Li and Si is neglected in our KMC method.

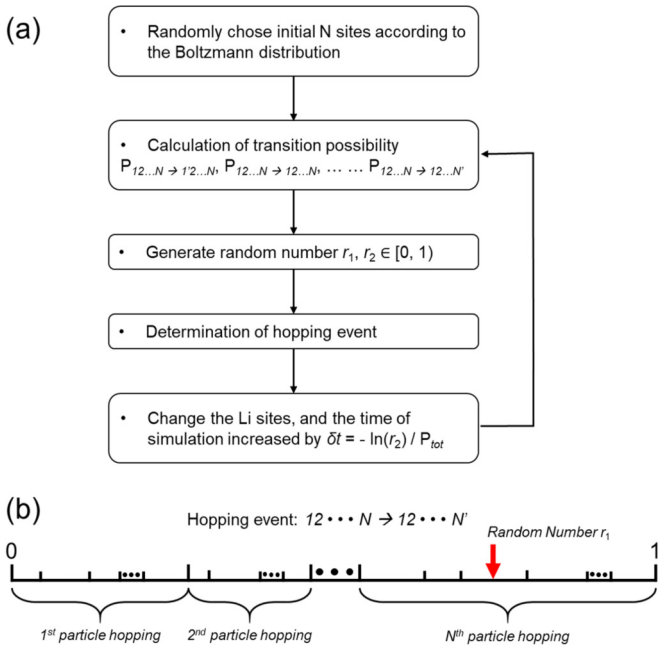

FIG. 2. Illustration of multiparticle kinetic Monte Carlo algorithm.

III. RESULTS AND DISCUSSION

A. Li/Si binary NN potential

The reference database for constructing the NN potential for the binary Li/Si system includes the DFT energies of 66 305 structures. It contains 49 544 pure Si data points from earlier work to construct the NN potential for *a*-Si [33]. 16 761 new reference data points for the binary system were sampled using the adaptive learning method and were included for the accurate description of Li-Si interaction. Approximately 10% of these structures were set aside for validation purposes in the test set. The contents of the reference database are provided in the Supplemental Material [48].

The chemical environments of Li and Si were represented by 52 and 104 symmetry functions, respectively, in the Si/Li binary NN potential, and the cutoff radius of symmetry functions was set to 6.0 Å. Several NN potentials with various numbers of neurons in the three hidden layers were generated, and that employed atomic NNs with 20 neurons per hidden layer exhibited the smallest energy and force RMSE values. Thus, we selected this NN potential for the following simulation. The energy and force prediction errors in the training/testing set are provided in Table I. We observed that the energy and force prediction were more accurate for binary structures as many high-temperature liquid-phase Si reference structures were included in the training data, which compromises the energy prediction accuracy to a certain extent.

As a first test of the NN potential, we calculated the radial distribution function (RDF) of a Li/*a*-Si structure at 300 and 900 K. The results are presented in Fig. 3(a) and are compared with those obtained from *ab initio* MD. The initial structure consisted of 64 atoms of the *a*-Si matrix and 1 Li atom, and the MD simulations were run for 10 ps. The RDF obtained from the NN was very close to the DFT data. Another preliminary validation was performed using the NEB method to calculate the Li diffusion pathway in *c*-Si using both the NN potential and the *ab initio* method. The energy profiles are presented in Fig. 3(b). Although most of the reference structure was sampled from the *a*-Si matrix, the Li diffusion barrier in the crystal was accurately predicted using the NN potential (NN potential: 0.52 eV; DFT: 0.56 eV).

Then, we tested the reliability of the NN potential in constructing the Li *diffusive network* (including stable interstitial positions, connectivity, diffusion pathways, and barrier energies) in *a*-Si matrix. In this test, a small-size (64 atoms) *a*-Si model was first generated using the melt-quenching process at a slow cooling rate (10^{11} K/s). Then, the *diffusive network* for Li was thoroughly searched with the NN potential using the method introduced in Sec. II B. We obtained 36 stable sites and 81 hopping paths from the small-size *a*-Si model. Then, the interstitial positions were further optimized based on *ab initio* calculations. The interstitial Li atoms were displaced by 0.19 Å during the *ab initio* optimization process.

Another important property that has a significant effect on diffusion behavior is the binding energy between the Li atom and amorphous matrix. Usually, the formation energy of a Li interstitial is defined as $E_{\text{formation}} = E_{\text{total}} - E_{a-\text{Si}} - E_{\text{singleLi}}$, where E_{total} is the energy of the *a*-Si model with one interstitial Li, $E_{a-\text{Si}}$ is the energy of the *a*-Si matrix, and E_{singleLi} is the energy of one Li atom from the crystalline phase. The binding energy is the negative of the interstitial formation energy, and thus, a larger binding energy indicates that a Li atom is more strongly bound to the interstitial site. However, because the NN potential is not trained with bulk Li structures, the accurate calculation of E_{singleLi} using the NN potential is difficult. In this work, we simply assumed that E_{singleLi} is zero, i.e., $E_{\text{binding}} = E_{a-\text{Si}} - E_{\text{total}}$. The Li binding energies obtained from the NN potential and *ab initio* calculations are presented in Fig. 4(a), and the mean absolute error of the NN potential calculation is 0.098 eV. The diffusion paths were calculated using the *ab-initio*-based NEB method with the *ab-initio*-optimized interstitial configurations used as the initial and final states. The Li binding energies computed using both methods are presented in Fig. 4(a), and the mean absolute error was 0.098 eV. The barrier energy of the

TABLE I. Energy and force prediction error of NN potential.

	Number of structures	Energy (meV/atom)		Force (eV/Å)	
		Train	Test	Train	Test
Si	44518	5.21	5.80	0.248	0.245
Li/Si	16761	1.61	1.64	0.198	0.201
Total	61279	4.23	4.66	0.234	0.233

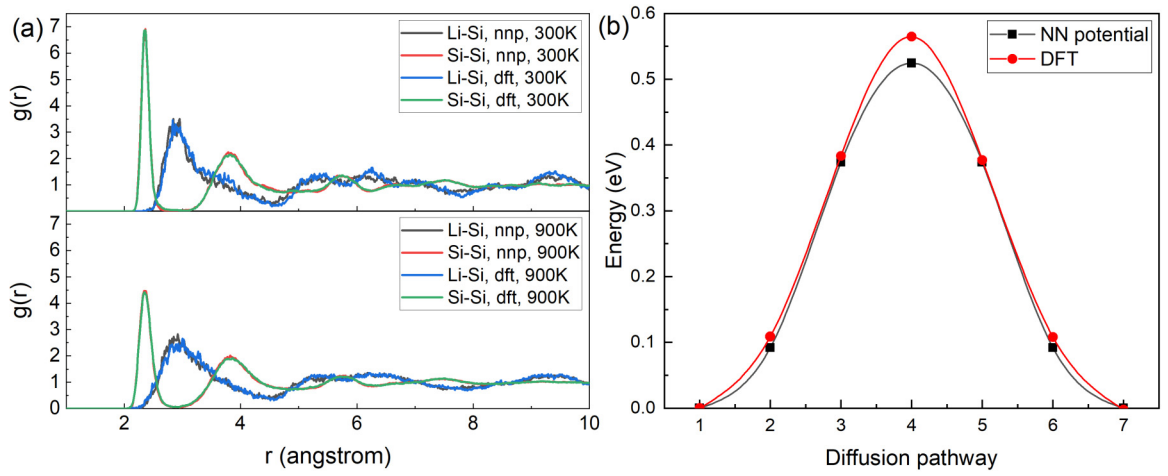

FIG. 3. (a) Si–Si and Li–Si radial distribution functions obtained from NN potential-based MD and *ab initio* MD. (b) Diffusion barrier energies of a single Li atom in the crystal Si obtained from NEB method.

interstitial diffusion paths is plotted in Fig. 4(b), and the mean absolute error was 0.17 eV. These results indicate that the NN potential can reproduce the *ab initio* results reasonably well in calculating the diffusive network of a Li atom.

B. Li diffusive network in *a*-Si matrix with various extents of structural order

In our earlier work, the atomic configurations of *a*-Si with different extents of structure order were determined by simulating cooling from the melt at different cooling rates ($10^{11}-10^{15}$) using the NN potential. The structural, energetic, and vibrational properties of *a*-Si models significantly shifted as a function of the cooling rate. A comprehensive comparison with experiments indicated that the theoretical model of low/high cooling rate corresponds to experimental sample annealing at high/low temperatures. In this work, we adopted the *a*-Si models created using 10^{11}, 10^{12}, and 10^{13} K/s in our earlier work and generated three additional *a*-Si models using 3×10^{11}, 3×10^{12}, and 3×10^{13} K/s. All the models contained 512 Si atoms. The excess energies of these *a*-Si models are listed in Table II. The excess energy is approximately comparable to the experimental measurement of the crystallization enthalpy ΔH, and the excess energies of all the above models are within the experimental range of the ion-implantation samples (as-implanted and annealed at 150–500 °C), that is, 0.136–0.195 eV. The models of 10^{14} and 10^{15} K/s were not taken into consideration as their excess energy exceeded the experimental range.

The Li *diffusive network* in these *a*-Si models was calculated using the NN potential. To construct Li *diffusive networks* in the five *a*-Si models, we performed approximately more than 10^5 times of structure optimizations and more than 4000 times of NEB calculations in large supercells. Such a huge amount of computation is overwhelming for conventional DFT calculations, but can be done with the help of ML-based atomistic simulations. Figure 5(a) provides an illustration of the *diffusive network* in the highly ordered *a*-Si model (10^{11}K/s). The Li interstitial positions and diffusion pathways are represented by spheres and cylinders, respectively, and the binding energies of interstitial Li and saddle point energies of the diffusion pathways are indicated by different colors. We can see that the connectivity of the diffusion pathways is highly disordered and that the binding and barrier energies vary over a wide range.

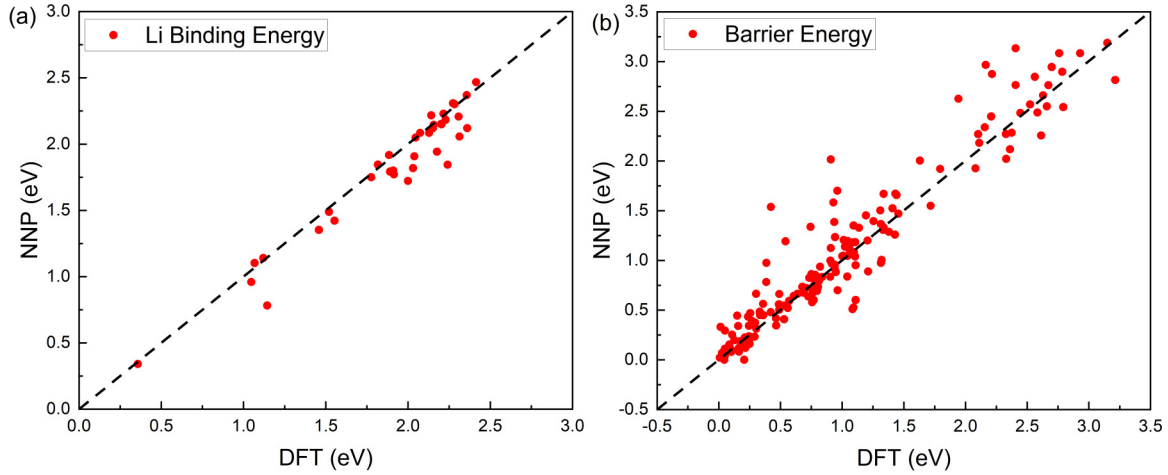

FIG. 4. Comparison of NN potential and *ab initio* calculations in calculation of key properties of Li diffusion potential energy surface: (a) Li binding energy and (b) barrier energy of Li diffusion.

TABLE II. Excess energy, number of stable interstitial positions, and number of diffusion pathways in *a*-Si models generated using different cooling rates.

Cooling rate (K/s)	10^{11}	3×10^{11}	10^{12}	3×10^{12}	10^{13}	3×10^{13}
Excess energy (eV)	0.138	0.140	0.148	0.152	0.171	0.185
No. of stable sites	350	323	316	317	316	304
No. of diffusion paths	732	706	705	700	701	690

The number of stable interstitial positions in *a*-Si models (listed in Table II) varies between 304 and 350, with the ordered model tending to have more stable sites. The concentration of Li interstitial sites is in the range of 0.6–0.7, which is close to the findings of Tritsaris's first-principles study [13], in which 32 equilibrium sites for the Li interstitial were observed in a small *a*-Si model containing 64 Si atoms.

The distribution of the Li binding energy in different *a*-Si models is shown in Fig. 5(b). For ease of visualization, each of the discrete binding energies was plotted using a Gaussian distribution with 0.01-eV width. The binding energies of most Li equilibrium sites are in the range of 1.5–2.5 eV, with a few sites having lower binding energies. We were not able to locate available data from previous research that could be used for comparison. However, the distribution shows reasonable agreement with that of previous validation *ab initio* calculations in the small *a*-Si model (Sec. III A). In Fig. 5(d), the average binding energies in different *a*-Si models are plotted against the excess energy of the *a*-Si models, which is an indicator of the degree of structural disorder. As expected, the binding between Li and the a-Si matrix is weaker (stronger) in the more highly ordered (disordered) atomic environment. As coordination defects and large voids are present in the highly disordered *a*-Si structures, they facilitate stronger binding between Li and Si atoms. Detailed analysis is provided in Sec. III D.

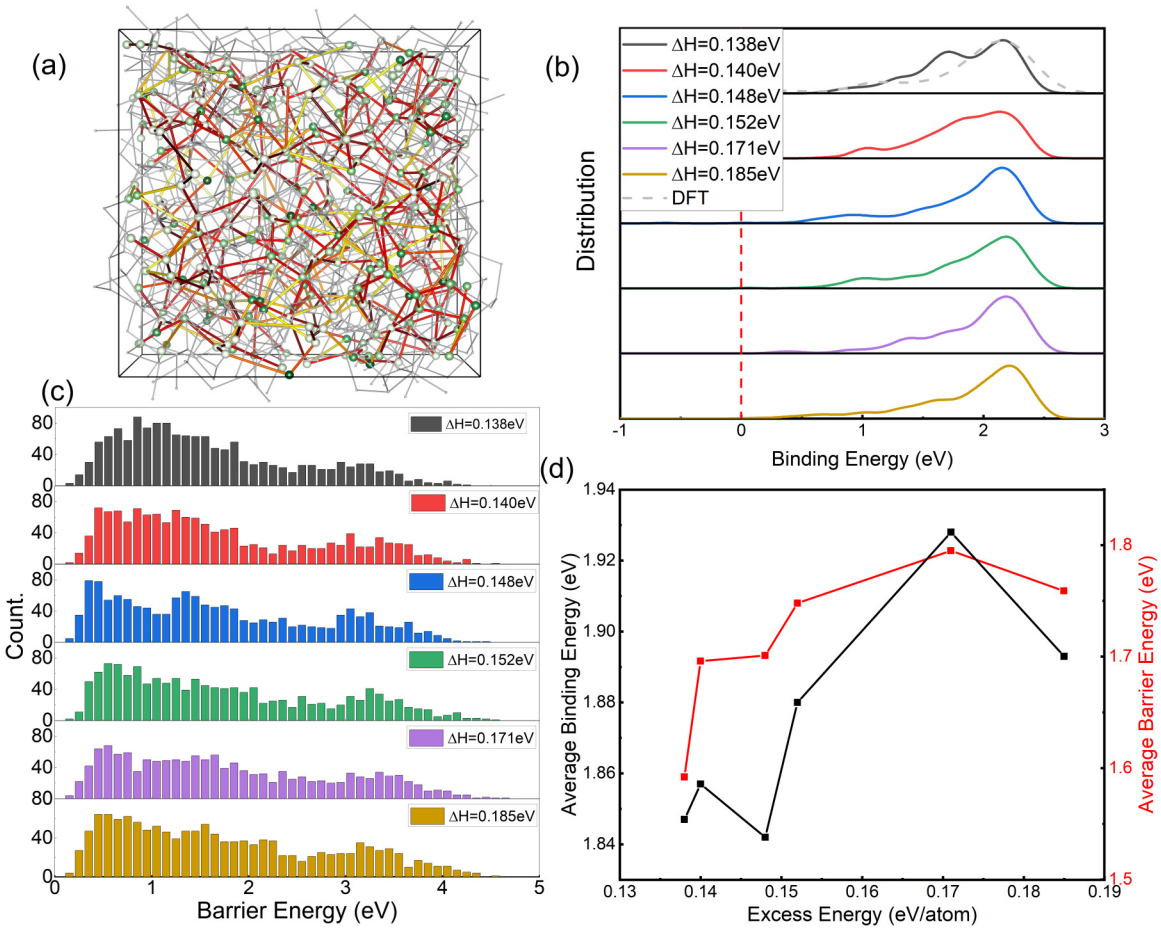

FIG. 5. Diffusive networks in *a*-Si models computed using NN potential. (a) Location of equilibrium site and diffusion path of Li interstitial in *a*-Si model. The *a*-Si contains 512 atoms and was generated using a cooling rate of 1011 K/s. The binding energy of the equilibrium site is indicated by the color (dark green: strongly bound sites; light green: weakly bound sites). The saddle point energy of the diffusion path is also indicated by the color (red: low saddle point energy; yellow: high saddle point energy). The *a*-Si matrix is represented by the light-gray network. (b) Distribution of binding energy of Li equilibrium in different *a*-Si models. (c) Distribution of barrier energy of Li interstitial pathways in different *a*-Si models. (d) Average binding energy and barrier energy in different *a*-Si models.

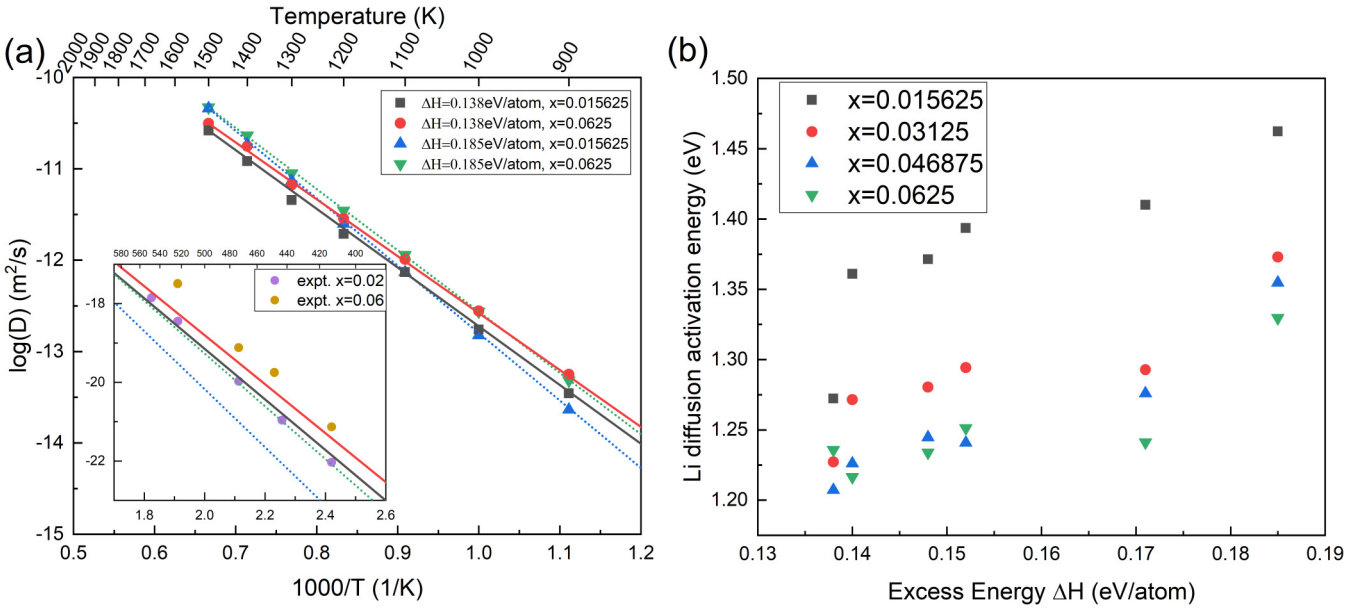

FIG. 6. Li diffusion properties in different *a*-Si models: (a) Arrhenius plot of Li diffusivity and (b) Li diffusion activation energy.

These interstitial positions are connected in the *diffusive network* by 690–732 diffusion pathways in the different *a*-Si models. The distribution of the barrier energies of the diffusion pathways is shown in Fig. 5(c). Most diffusion pathways have barrier energies between 0.1 and 2.5 eV, which is in excellent agreement with Tritsaris's first-principles results [13]. However, we also observed a few diffusion pathways with barrier energies higher than 2.5 eV. Our method to construct a *diffusive network* involved thoroughly searching all the possible pathways present on the PES, including those with very high barriers that an atom would be very unlikely to hop through in a realistic diffusion process. Considering only pathways with barrier energies lower than 2.5 eV, the average number of neighboring hoping sites was 3.15–3.32, which is close to the number determined by Tritsaris's calculation, 2.87 [13]. The average barrier energies in different *a*-Si models are plotted in Fig. 5(d); it is apparent that the barrier energy of Li diffusion increased with increasing disorder of the local structure.

C. Li diffusion behavior

The diffusivity of Li in different *a*-Si matrices was examined by performing KMC simulations. To account for the effect of Li concentration, multiple diffusing Li atoms were added to the *diffusive network*. The number of Li atoms were 8, 16, 24, and 32, and the Li concentration was $x = 0.0156$, 0.0312, 0.0469, and 0.0625. The KMC simulations were performed at 900, 1000, 1100, 1200, 1300, 1400, and 1500 K, and the Li diffusivity at different temperatures was calculated using

$$D = \lim_{t\to\infty} \frac{1}{6t}|r(t) - r(0)|^2.$$

The Li diffusivities in the most ordered ($\Delta H = 0.138$ eV) and most disordered ($\Delta H = 0.185$ eV) *a*-Si models are plotted in Fig. 6(a). In our previous work, we demonstrated that the most ordered *a*-Si model showed excellent agreement with a well-annealed experimental sample in terms of the structural factor, radial distribution function, excess enthalpy, and Raman spectrum [33]. The activation energies of Li diffusion in this *a*-Si model could be estimated by fitting the Arrhenius law. The Li diffusion activation energy was estimated to be 1.27 eV for a Li concentration of $x = 0.0156$. This value slightly decreased to 1.23 eV upon increasing the Li concentration to $x = 0.0625$. The calculated activation energies were in good agreement with SIMS experimental measurements within a similar range of Li concentration, 1.46 eV for $x = 0.02$ and 1.38 eV for $x = 0.06$ [10]. To facilitate the direct comparison of the Li diffusivity between simulation and experiment, the Arrhenius plot of the KMC simulation was extrapolated to a lower temperature range that matched that of the experiment (140–325 °C). The Li diffusion coefficient ($x = 0.0156$) varied between 8.5×10^{-18} m^2/s and 1.3×10^{-22} m^2/s in the experimental temperature range, which is in excellent agreement with the SIMS measurement range of 10^{-17}–10^{-22} m^2/s ($x = 0.02$). The current model and methods neglected the lattice volume expansion caused by Li insertion. In this work, the *a*-Li$_x$Si phase with very low Li concentration ($x = 0.0156 - 0.0625$) is investigated. Due to the low Li concentration, the lattice volume expansion would be small.

In the most disordered *a*-Si model, the Li activation energy was estimated to be 1.46 eV at lower Li concentration and 1.33 eV at higher concentration. The activation energies were substantially increased by the disordering of the amorphous matrix. The increasing activation energy can be explained with the "trap" mechanism of Li diffusion, which is introduced in detail in Sec. III D. In both the most ordered and most disordered *a*-Si matrices, the diffusivity is enhanced with increasing Li concentration. This phenomenon was also observed in the SIMS experiment.

To provide a comprehensive explanation of how concentration and local disorder affect Li diffusion behavior, the activation energies of Li diffusion in the six *a*-Si models at

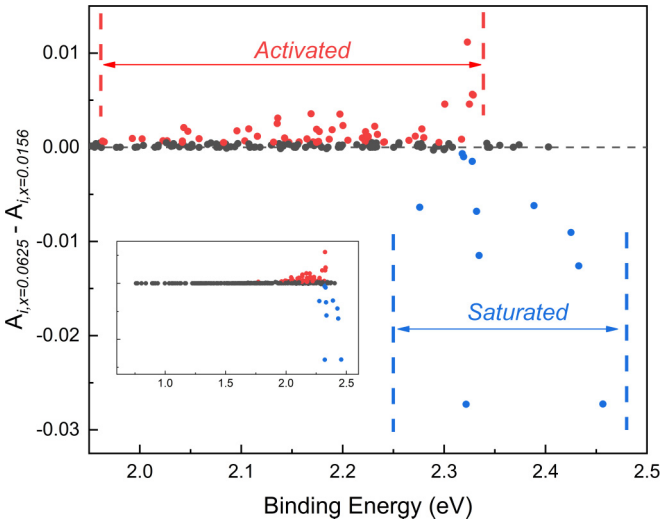

FIG. 7. Change of activity of Li interstitial sites in KMC simulation ($A_{i,x=0.0625} - A_{i,x=0.0156}$) upon increasing Li concentration from $x = 0.0156$ to 0.0625. The a-Si model was generated at a cooling rate of 10^{11} K/s. The red (blue) sites are significantly more active (less active) as the Li concentration increases. The activity of Li sites with low binding energy (<1.95eV) is only shown in the inset because they rarely participate in the transport process.

different Li concentrations are plotted in Fig. 6(b). It is apparent that (1) the Li diffusion activation energy increases with increasing disorder of the a-Si matrix and (2) the Li diffusion activation energy decreases with increasing Li concentration.

D. Trap mechanism

A high Li concentration leads to faster Li diffusion in a-Si, as observed both experimentally [10] and in theoretical calculations (this work). The most likely explanation for the acceleration of diffusion is the "trap-limited" diffusion mechanism. The Li atom in some interstitial positions is strongly bound to the amorphous matrix (high binding energy). The Li atom is easily trapped in these sites and has difficulty escaping. It is assumed that the higher Li concentration leads to more saturated trap sites, and hence, Li diffusion is accelerated. To obtain evidence supporting the trap mechanism, we defined the concept of "activity" of a site, which was estimated from the KMC trajectory. The activity A_i of a site "i" is given by the count of hopping events to (from) the site i divided by the total number of hopping events during a certain period. In other words, for higher activity A_i, the interstitial site i will play a more important role in the transport process. We analyzed the activity of each site in the diffusive network of the "most ordered" a-Si model [as shown in Fig. 5(a)] at 1500 K. Figure 7 shows how the activity of each sites changes when the Li concentration increases from $x = 0.0156$ to 0.0625, i.e., $A_{i,x=0.0625} - A_{i,x=0.0156}$. If this value is negative, the activity of such a site decreases as the Li concentration increases, and *vice versa*. The activity of interstitial sites strongly bound to the amorphous matrix (binding energies of 2.25–2.5 eV) was observed to decrease with increasing Li concentration. However, interstitial sites with relatively high binding energies (2.0–2.35 eV) became more active when the Li concentration was high. Our observation in the KMC simulation supports the experimental speculation that the strongly bound interstitial sites, i.e., trap sites, are saturated when the Li concentration is high such that the diffusion of other Li atoms will not be hindered by these sites.

One important task is identification of the atomistic origins of the Li traps. Experimentalists have speculated that the coordination defects of a-Si might be traps of Li ions [9,10,12]. In this work, the interaction between Li interstitials and coordination defects was analyzed in detail using the "most ordered" a-Si model [(as shown in Fig. 5(a)]. We classified the Li sites into three types: (I) binding to the dangling bond (3-coordinated Si atom), (II) binding to a floating bond (5-coordinated Si atom), or (III) only binding to nondefective (four-coordinated) Si atoms. Type I/II sites were defined as Li sites with at least one neighboring dangling/floating bond Si atom within a cutoff distance of 3 Å. The distributions of the binding energy in different classes are plotted in Fig. 8(a). As expected, the binding energy of Li sites neighboring a dangling bond is distributed mainly in the higher energy range. The average binding energy of type I was 2.03 eV, which is 0.22-eV stronger than that of Li sites surrounded by nondefective Si atoms. This result supports the conjecture that dangling bonds might serve as traps of Li ions in a-Si.

A deeper reason why Li ions are easily trapped by dangling-bond Si is related to the nature of the Si–Li bond. First-principles calculation was performed to identify the electronic properties of the Si–Li bond. To facilitate the first-principles calculation, we again used the small-size (64 atoms) a-Si structure used to validate the reliability of the NN potential in Sec. III A. The Li interstitial structures were optimized using the first-principles method, and then, the electronic localization function (ELF) [60] of the optimized interstitial structures was calculated. Figure 8 presents the ELF plots around two interstitial Li atoms: one (left panel) is neighboring a dangling bond Si, and the other (right panel) is only neighboring nondefective Si. The value of ELF ranges from 0 to 1, where 1 corresponds to localization as in covalent bonds and 0.5 corresponds to the electron-gas-like pair probability as in metallic bonds; thus, analysis of ELF can effectively reveal the nature of different chemical bonds. The bond between Li and the dangling-bond Si somehow exhibited the nature of a covalent bond, as indicated by the red region in the middle of the Li–Si bond. However, the bond between Li and other nondefective Si atoms did not show such a characteristic. In general, Li ions are easily trapped by the dangling-bond Si because Li and the dangling-bond Si form covalentlike bonds, which have higher bond energy than normal Li–Si bonds.

However, we observed inconsistency between the experimentally estimated trap energy of 0.7–1.0 eV and that of the dangling bond, 0.22 eV. This finding implies that there may be another atomic origin of Li-ion traps. Here, we analyzed the contribution of large-volume voids in the a-Si matrix. The void volume of one interstitial site was estimated from the Voronoi segment. Figure 9 shows the clear correlation between the void volume and binding energy of Li interstitial sites in different a-Si models. As expected, the Li has higher binding energy in the large-volume voids. Thus, large-volume voids may be another source of Li "traps".

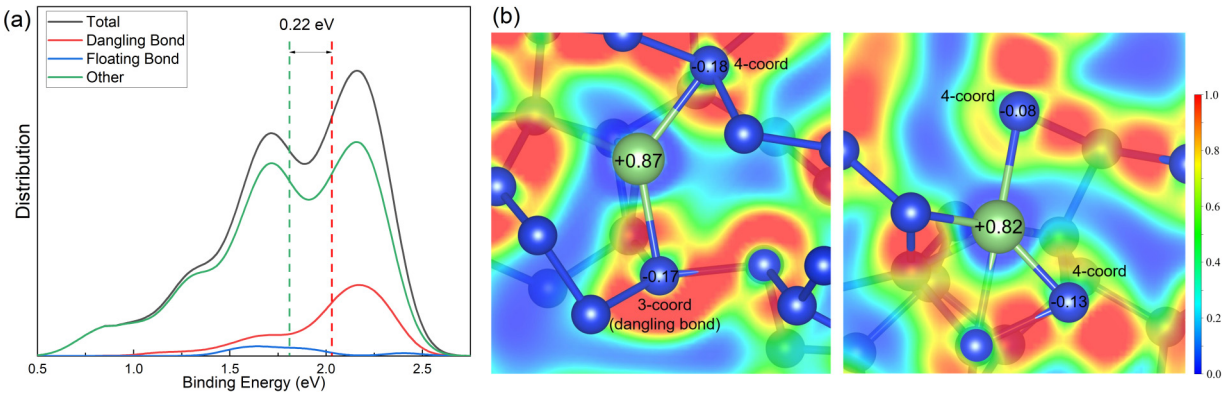

FIG. 8. (a) Distribution of binding energy of different types of Li interstitial sites in *a*-Si model generated using cooling rate of 10^{11} K/s. (b) ELF of Li/*a*-Si structures. (Left panel) Li bonding to one-dangling-bond Si atoms. (Right panel) Li bonding to nondefective Si atoms. The numbers indicate the Bader charges of Li and Si atoms.

The Li ions are easily trapped by (I) dangling-bond Si and (II) large volume voids. The effect of local structure order on the Li diffusion activation energy can be explained from this perspective: the highly disordered *a*-Si matrix contains more dangling bonds and larger voids, and a higher trap density corresponds to a higher Li diffusion activation energy. Previous studies have shown that highly disordered structures contain more coordination defects [33,40,61,62]. In addition, large-volume voids are likely to form in highly disordered structures because of the inhomogeneous distribution of atom positions. As illustrated in Fig. 9 (bottom panel), the concentration of large-volume voids is high in the highly disordered *a*-Si model.

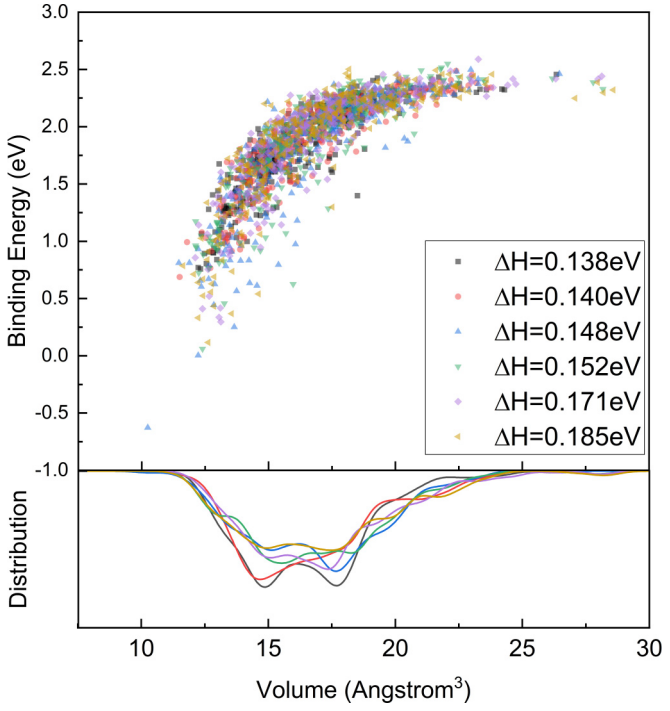

FIG. 9. Top: Correlation between void volume of Li interstitial sites and binding energy. Bottom: Distribution of void volume in different *a*-Si models.

This work focused on the explanation of Li diffusion mechanism in *a*-Si anode with an ideal bulk system, while an actual battery system has a much more complicated structure including the interfaces between electrode and electrolyte. Moreover, conditions under bias voltage also make a significant influence on the Li diffusion behavior in batteries. Further study is necessary to address these factors.

IV. CONCLUSIONS

In this work, the high-dimensional NN potential was built for the Li/Si binary system and was used to characterize the effect of local structure order on the interstitial Li diffusion behavior. First, a series of *a*-Si models with different degrees of disorder were generated by simulated cooling from the melt at different cooling rates. Then, the Li *diffusive network*, including the diffusion pathways and topology of connectivity, inside the *a*-Si models was calculated. Finally, the Li diffusivities were estimated from KMC simulations. We proposed a method to comprehensively and unambiguously build the *diffusive network*, which involved a combination of PES presampling and NEB calculations. In addition, the multiparticle KMC algorithm was used to account for the effect of Li concentration.

For a Li concentration of $x = 0.0156$, the diffusion activation energy increased from 1.27 to 1.46 eV with the structural order changing from highly ordered to highly disordered. When the Li concentration was higher, $x = 0.0625$, identical dependence of the activation energy on the structural order was observed, with the energy varying from 1.23 to 1.33 eV. The diffusion activation energies were much higher than that in *c*-Si, 0.55 eV, but were consistent with experimental values, 1.38–1.46 eV. In addition, we observed that the Li diffusivity was enhanced when the Li concentration increased from $x = 0.0156$ to $x = 0.0625$, which was also consistent with experimental observations.

The effect of local structure order and Li concentration on the diffusion properties can be explained by the *trap mechanism*. From the analysis of KMC trajectories, we observed that the trap sites, which have very high Li binding energies, are saturated when the Li concentration in the diffusive network is high. This situation avoids the other Li ions being captured by

trap sites, and hence, the overall Li diffusion becomes faster. The atomistic origins of the trap sites were also investigated. Dangling-bond Si atoms were observed to be more likely to trap Li ions as the first-principles ELF indicates that a Si–Li bond with dangling bonds has a more strongly covalent nature. In addition, a clear correlation between the binding energy and void volume of Li interstitials was observed, with larger-volume interstitial sites having higher binding energy. Therefore, large-volume voids in an *a*-Si matrix serve as another origin of Li trap sites. The highly disordered *a*-Si matrix tends to have a high concentration of dangling bonds and large voids. Consequently, the Li diffusion activation energy is high in the highly disordered *a*-Si model.

ACKNOWLEDGMENTS

This paper is based on results from a project (No. P16010) commissioned by the New Energy and Industrial Technology Development Organization (NEDO). We thank T. Jain, M.S., from Edanz Group [63] for editing a draft of this manuscript.

[1] G. Jeong, Y.-U. Kim, H. Kim, Y.-J. Kim, and H.-J. Sohn, Energy Environ. Sci. **4**, 1986 (2011).
[2] U. Kasavajjula, C. Wang, and A. J. Appleby, J. Power Sources **163**, 1003 (2007).
[3] L. A. Berla, S. W. Lee, I. Ryu, Y. Cui, and W. D. Nix, J. Power Sources **258**, 253 (2014).
[4] X. Xiao, P. Liu, M. W. Verbrugge, H. Haftbaradaran, and H. Gao, J. Power Sources **196**, 1409 (2011).
[5] T. L. Kulova, A. M. Skundin, Y. V. Pleskov, E. I. Terukov, and O. I. Kon'kov, J. Electroanal. Chem. **600**, 217 (2007).
[6] J. Xie, N. Imanishi, T. Zhang, A. Hirano, Y. Takeda, and O. Yamamoto, Mater. Chem. Phys. **120**, 421 (2010).
[7] N. Ding, J. Xu, Y. X. Yao, G. Wegner, X. Fang, C. H. Chen, and I. Lieberwirth, Solid State Ionics **180**, 222 (2009).
[8] J. Li, X. Xiao, F. Yang, M. W. Verbrugge, and Y.-T. Cheng, J. Phys. Chem. C **116**, 1472 (2012).
[9] E. Hüger and H. Schmidt, J. Phys. Chem. C **122**, 28528 (2018).
[10] F. Strauß, L. Dörrer, M. Bruns, and H. Schmidt, J. Phys. Chem. C **122**, 6508 (2018).
[11] K. Wen, M. Xia, P. Deng, W. Lv, and W. He, Chem. Eng. Sci. **200**, 80 (2019).
[12] E. Hüger, L. Dörrer, and H. Schmidt, Chem. Mater. **30**, 3254 (2018).
[13] G. A. Tritsaris, K. Zhao, O. U. Okeke, and E. Kaxiras, J. Phys. Chem. C **116**, 22212 (2012).
[14] X. Yan, A. Gouissem, and P. Sharma, Mech. Mater. **91**, 306 (2015).
[15] P. Johari, Y. Qi, and V. B. Shenoy, Nano Lett. **11**, 5494 (2011).
[16] C. Chang, X. Li, and Z. Xu, Appl. Phys. Lett. **113**, 121904 (2018).
[17] J. Behler and M. Parrinello, Phys. Rev. Lett. **98**, 146401 (2007).
[18] N. Artrith, A. Urban, and G. Ceder, Phys. Rev. B **96**, 014112 (2017).
[19] A. P. Bartók, M. C. Payne, R. Kondor, and G. Csányi, Phys. Rev. Lett. **104**, 136403 (2010).
[20] A. P. Thompson, L. P. Swiler, C. R. Trott, S. M. Foiles, and G. J. Tucker, J. Comput. Phys. **285**, 316 (2015).
[21] A. Seko, A. Takahashi, and I. Tanaka, Phys. Rev. B **90**, 024101 (2014).
[22] H. Huo and M. Rupp, arXiv:1704.06439 (2017).
[23] M. Rupp, A. Tkatchenko, K.-R. Müller, and O. A. von Lilienfeld, Phys. Rev. Lett. **108**, 058301 (2012).
[24] W. Li, Y. Ando, and S. Watanabe, J. Phys. Soc. Jpn. **86**, 104004 (2017).
[25] W. Li, Y. Ando, E. Minamitani, and S. Watanabe, J. Chem. Phys. **147**, 214106 (2017).
[26] N. Artrith and A. Urban, Comput. Mater. Sci. **114**, 135 (2016).
[27] N. Artrith, A. Urban, and G. Ceder, J. Chem. Phys. **148**, 241711 (2018).
[28] K. V. J. Jose, N. Artrith, and J. Behler, J. Chem. Phys. **136**, 194111 (2012).
[29] C. Schran, F. Uhl, J. Behler, and D. Marx, J. Chem. Phys. **148**, 102310 (2018).
[30] T. T. Nguyen, E. Székely, G. Imbalzano, J. Behler, G. Csányi, M. Ceriotti, A. W. Götz, and F. Paesani, J. Chem. Phys. **148**, 241725 (2018).
[31] W. Jeong, K. Lee, D. Yoo, D. Lee, and S. Han, J. Phys. Chem. C **122**, 22790 (2018).
[32] D. Yoo, K. Lee, W. Jeong, D. Lee, S. Watanabe, and S. Han, Phys. Rev. Mater. **3**, 093802 (2019).
[33] W. Li and Y. Ando, J. Chem. Phys. **151**, 114101 (2019).
[34] M. Rupp, O. A. Von Lilienfeld, and K. Burke, J. Chem. Phys. **148**, 241401 (2018).
[35] R. Kobayashi, D. Giofré, T. Junge, M. Ceriotti, and W. A. Curtin, Phys. Rev. Mater. **1**, 53604 (2017).
[36] L. Zhang, D.-Y. Lin, H. Wang, R. Car, and W. E, Phys. Rev. Mater. **3**, 023804 (2019).
[37] A. S. Bochkarev, A. Van Roekeghem, S. Mossa, and N. Mingo, Phys. Rev. Mater. **3**, 93803 (2019).
[38] K. Miwa and R. Asahi, Phys. Rev. Mater. **2**, 105404 (2018).
[39] M. Rupp, R. Ramakrishnan, and O. A. von Lilienfeld, J. Phys. Chem. Lett. **6**, 3309 (2015).
[40] V. L. Deringer, N. Bernstein, A. P. Bartók, M. J. Cliffe, R. N. Kerber, L. E. Marbella, C. P. Grey, S. R. Elliott, and G. Csányi, J. Phys. Chem. Lett. **9**, 2879 (2018).
[41] D. Dragoni, T. D. Daff, G. Csányi, and N. Marzari, Phys. Rev. Mater. **2**, 13808 (2018).
[42] H. Babaei, R. Guo, A. Hashemi, and S. Lee, Phys. Rev. Mater. **3**, 074603 (2019).
[43] W. Li and Y. Ando, Phys. Chem. Chem. Phys. **20**, 30006 (2018).
[44] A. Seko, A. Takahashi, and I. Tanaka, Phys. Rev. B **92**, 054113 (2015).
[45] R. Ouyang, S. Curtarolo, E. Ahmetcik, M. Scheffler, and L. M. Ghiringhelli, Phys. Rev. Mater. **2**, 83802 (2018).
[46] J. Behler, Angew. Chem. - Int. Ed. **56**, 12828 (2017).
[47] J. Behler, J. Chem. Phys. **134**, 074106 (2011).
[48] See Supplemental Material at http://link.aps.org/supplemental/10.1103/PhysRevMaterials.4.045602 for detailed information of reference database and NN potential parameters.

[49] G. Kresse and J. Furthmüller, Phys. Rev. B **54**, 11169 (1996).
[50] M. Fuchs and M. Scheffler, Comput. Phys. Commun. **119**, 67 (1999).
[51] G. Kresse and D. Joubert, Phys. Rev. B **59**, 1758 (1999).
[52] J. P. Perdew, K. Burke, and M. Ernzerhof, Phys. Rev. Lett. **77**, 3865 (1996).
[53] A. A. Peterson, R. Christensen, and A. Khorshidi, Phys. Chem. Chem. Phys. **19**, 10978 (2017).
[54] V. Botu and R. Ramprasad, Int. J. Quantum Chem. **115**, 1074 (2015).
[55] T. L. Jacobsen, M. S. Jørgensen, and B. Hammer, Phys. Rev. Lett. **120**, 026102 (2018).
[56] Z. Li, J. R. Kermode, and A. De Vita, Phys. Rev. Lett. **114**, 096405 (2015).
[57] M. Gastegger, J. Behler, and P. Marquetand, Chem. Sci. **8**, 6924 (2017).
[58] S. Hao and C. Wolverton, J. Phys. Chem. C **117**, 8009 (2013).
[59] Y. Fan, A. Kushima, S. Yip, and B. Yildiz, Phys. Rev. Lett. **106**, 125501 (2011).
[60] A. D. Becke and K. E. Edgecombe, J. Chem. Phys. **92**, 5397 (1990).
[61] R. Atta-Fynn and P. Biswas, J. Chem. Phys. **148**, 204503 (2018).
[62] A. Pedersen, L. Pizzagalli, and H. Jónsson, New J. Phys. **19**, 063018 (2017).
[63] www.edanzediting.com/ac.